JMEPEG (2010) 19:1284–1289
DOI: 10.1007/s11665-009-9579-3

1059-9495/$19.00

Synergistic Effects of Hydrogen and Stress on Corrosion of X100 Pipeline Steel in a Near-Neutral pH Solution

C. Zhang and Y.F. Cheng

(Submitted June 22, 2009; in revised form September 10, 2009)

In this work, scanning vibrating electrode technique and local electrochemical impedance spectroscopy measurements were used to investigate the effects of stress and hydrogen on electrochemical corrosion behavior of a X100 pipeline steel in a near-neutral pH solution. The stress distribution on the test specimen was calculated using the finite element method. Results demonstrated that the hydrogen-charging enhances the local anodic dissolution of the steel, contributing to the formation of a layer of corrosion product. However, there is little difference of the charge-transfer resistance between the regions with and without hydrogen-charging due to rapid diffusion of hydrogen atoms throughout the specimen with time. When the local stress concentration is not significant enough to approach the yielding strength of the steel, the steel is still in a relatively stable state, and there is a uniform distribution of dissolution rate over the whole surface of the steel specimen. Although the stress-enhanced activation is not sufficient to result in an apparent difference of current density of the steel, the activation of the steel would activate dislocations, which serve as effective traps to the charged hydrogen atoms. With the increase of hydrogen concentration, the hydrogen-enhanced anodic dissolution becomes dominant.

Keywords corrosion, hydrogen-charging, micro-electrochemical measurements, near-neutral pH solution, stress, X100 pipeline steel

1. Introduction

In the recent years, with the continuously growing demand in energy consumption, extensive attentions have been paid to supply oil and natural oil in a more economic and safer way. Development of high-strength steel pipelines has enabled the energy industry to realize significant savings in the total cost of long-distance oil/gas transmission in view of the pipeline wall thickness and operating pressure (Ref 1, 2). While the highest-strength grade of pipelines that have so far been brought to commercial application is X80 by American Petroleum Institute (API), the worldwide leading steelmakers, such as Nippon Steel Corporation, were pursuing the development and commercial application of X100 steel pipelines (Ref 3). To date, development of high-strength steel pipeline technology has focused on improvement of strength and mechanical properties, achieving higher grades, without reducing toughness properties and weldability of the steels through thermomechanical and alloying treatments (Ref 4-6).

Corrosion and stress corrosion cracking (SCC) have been identified as main reasons resulting in pipeline failure. Study on the electrochemical corrosion and SCC behavior of high-strength line pipe steels has been conducted recently. For example, Zheng et al. (Ref 7, 8) investigated SCC of X80 and X100 steels in a near-neutral pH soil solution, and found that SCC of the steels at high-stress level under quasi-static condition has a considerable incubation for initiation. Cracks continue to grow and new cracks continue to develop as the test time increases. Almonsour (Ref 9) investigated the sulfide SCC of X100 steel in a H_2S environment. It was found that the addition of H_2S enhanced the anodic kinetics. Moreover, the cathodic half cell potential increased, which shifted the cathodic polarization curve to higher current densities. SCC nucleated at corrosion pits on the metal surface and microcracks in the metal body and propagated perpendicular to the applied stress. HIC cracks nucleated at banded martensite-ferrite interfaces and propagated along the rolling direction parallel to the applied tensile stress through the softer ferrite phase.

It has been acknowledged (Ref 10-14) that buried pipelines generally experience two types of SCC, i.e., high pH SCC and near-neutral pH SCC. High pH SCC, usually resulting in an intergranular cracking, generally occurs in the presence of a concentrated carbonate/bicarbonate environment and at a pH greater than 9 (Ref 10-12). Moreover, high pH SCC is attributed to anodic dissolution at the grain boundaries and repeated rupture of passive films that form over the crack-tip. The occurrence of near-neutral pH SCC in natural gas pipelines is always associated with electrolyte characterized with anaerobic, dilute solutions (of the order of 0.01 M bicarbonate ions) with pH in the range of 6 to 7.5, and the stress corrosion crack has a transgranular, quasi-cleavage crack morphology with very little branching (Ref 10-30). Furthermore, it is proposed that the near-neutral pH SCC process involves anodic dissolution and, simultaneously, the ingress of hydrogen into steel. For example, Parkins (Ref 10) confirmed that hydrogen could discharge at cathode in near-neutral pH

C. Zhang, Department of Mechanical Engineering, University of Calgary, Calgary, AB T2N 1N4, Canada and Department of Materials Physics, University of Science and Technology Beijing, Beijing 100083, China and **Y.F. Cheng**, Department of Mechanical Engineering, University of Calgary, Calgary, AB T2N 1N4, Canada. Contact e-mail: fcheng@ucalgary.ca.

SCC in pipeline steels. He concluded that some synergistic effects between the hydrogen and anodic dissolution exist during the growth of near-neutral pH SCC of pipelines. Cheng (Ref 14) developed a thermodynamic model to illustrate the interactions of stress, hydrogen, and anodic dissolution at the crack-tip. It is shown that the growth rate of stress corrosion cracks under near-neutral pH condition depends on the effect of hydrogen on local anodic dissolution of steel in the absence of stress, the effect of stress on local anodic dissolution of steel in the absence of hydrogen, and the synergistic effect of hydrogen and stress on the anodic dissolution rate of steel at crack-tip.

While a significant number of works have been performed to investigate pipeline SCC, study of corrosion and SCC behavior of high-strength line pipe steel has been in its infancy. In this work, the effects of stress and hydrogen on electrochemical corrosion behavior of a X100 pipeline steel were investigated in a near-neutral pH solution by scanning vibrating electrode technique (SVET) and local electrochemical impedance spectroscopy (LEIS) measurements. The stress distribution on the test specimen was calculated using the finite element method.

2. Experimental

2.1 Electrodes and Solution

Specimen for electrochemical tests was cut from a sheet of API X100 steel pipe, with the chemical composition (wt.%): C 0.07, Mn 1.76, S 0.005, Si 0.10, P 0.018, Ni 0.154, Cr 0.016, Mo 0.20, V 0.005, Cu 0.243, and Al 0.027. The specimen was machined into a shape shown in Fig. 1(a), with a 10 by 10 by 10 mm dimension and a 49° V-type notch. The specimen was then loaded at 1000 N through a bolt-loading device as shown in Fig. 1(b), where the top surface of the specimen was shown. Four pieces of polymethyl-methacrylate insulating rods were installed in the gaps between specimen and the device to avoid their direct contact. The working surface of the specimen was ground sequentially to 1000 grit emery paper, and polished with 3 and 1 μm diamond pastes.

The test solution included a NS4 solution, which was used extensively to simulate the near-neutral pH electrolyte trapped under disbonded coating, with the chemical composition: 0.483 g/L $NaHCO_3$, 0.122 g/L KCl, 0.181 g/L $CaCl_2{\cdot}2H_2O$, and 0.131 g/L $MgSO_4{\cdot}7H_2O$. The solution pH was about 6.5 upon the continuous purging of 5% CO_2/N_2 gas. All the solutions were made from analytic grade reagents and ultrapure water (18 MΩ·cm in resistivity).

All the tests were performed at ambient temperature.

2.2 SVET and LEIS Measurements

The SVET and LEIS measurements were performed through a PAR 370 Scanning Electrochemical Workstation, which was described previously (Ref 27-30). A saturated calomel electrode (SCE) was used as reference electrode, and a platinum wire as auxiliary electrode. The micro-electrochemical scanning area was shown in Fig. 1.

For SVET and LEIS measurements on the charged specimen, the specimen was covered with a polythene adhesive tape, leaving a line with 0.5 mm in width for hydrogen-charging at −1.2 V (SCE) for 1 h in NS4 solution. The tape was then removed and SVET scan was conducted. A video camera was

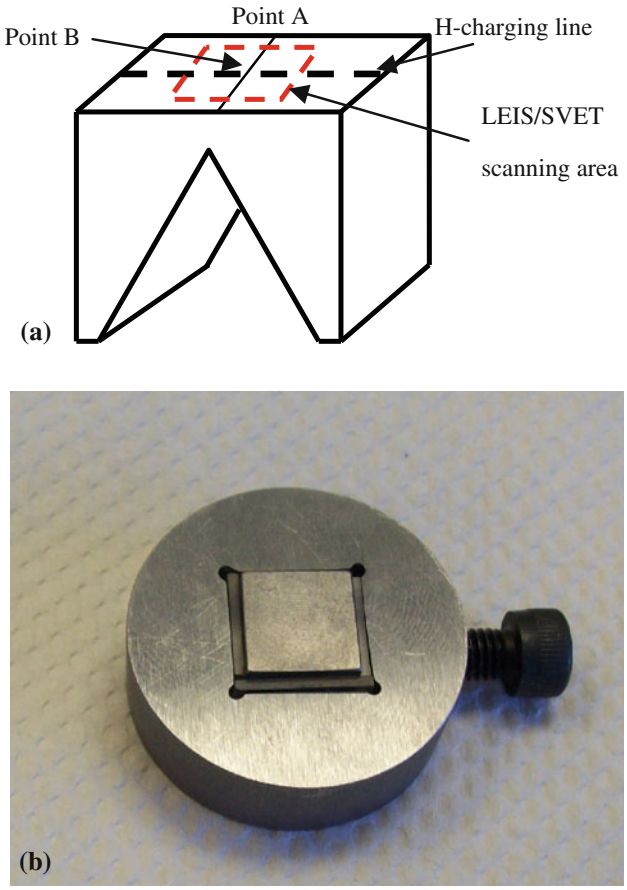

Fig. 1 Schematic diagram of the specimen (a) and the test rig (b)

used for imaging and controlling the distance between the Pt-Ir micro-probe and the work electrode surface, which was set at 100 μm. The vibrating amplitude of the micro-electrode was 30 μm and the vibrating frequency was 300 Hz in the direction normal to the surface. The potential of the microelectrode was proportional to its position in the vibrating plane. The difference of potentials when the microelectrode was located at the vibrating peak and valley, respectively, ΔE, was measured by an electrometer incorporated in M370. The solution resistance between the vibrating peak and valley, R, is determined by $R = d/k$, where d is the vibrating amplitude of the microelectrode (30 μm) and k is the solution conductivity. The SVET current, I, was then obtained by $I = \Delta E/R$. Therefore, what the SEVT measures is a potential, rather than a current. The current density plotted in the figures is actually a value based on the calculation shown above. A flat SVET current density diagram means that there is a uniform electrochemical activity of the test electrode, while a fluctuating SVET diagram is associated with an electrode with non-uniform electrochemical activity.

As stated previously, the LEIS measurements were operated in two modes: point measurement over a frequency range of 60,000 to 0.5 Hz, and area scanning at a fixed frequency of 10 Hz. An AC disturbance signal of 20 mV was applied to the electrode which was at corrosion potential. During LEIS point measurement, the microprobe with a 10 μm tip was set directly above the site to measure the typical impedance response at the individual point. The distance between the probe-tip and the

WE surface was approximately 50 μm, which was adjusted and monitored through the video camera TV system. For LEIS mapping, the microprobe was stepped over a designated area of the electrode surface. The scanning took the form of a raster in *x*-*y* plane. The step size was controlled to obtain a plot of 16 by 12 lines.

2.3 Computational Simulation of Stress Distribution

Computational simulation of the stress distribution in the pre-cracked specimen under applied force was conducted using a commercial software package COSMOSworks 2007 Service Pack. Detailed mesh conditions were listed as follows:

(1) Mesh type: Solid type
(2) Mesher Used Standard
(3) Jacobian check for solid: 4 points
(4) Element size: 0.778936 mm
(5) Maximum aspect ratio: 4.0536

3. Results

3.1 Computational Simulation of Stress Contribution of the Specimen

Figure 2 shows the simulated distribution of stress on the specimen under an applied load of 1000 N, where both 3D and linear diagrams were given. A maximum stress of about 6.4×10^8 N/m^2 (~640 MPa) was observed at the notch line, and the stress decreased rapidly with the increasing distance from the notch.

3.2 LEIS Measurements

Figure 3 shows the LEIS plots measured at two points (points A and B as shown in Fig. 1) along the notch line on the specimen surface in NS4 solution, where point B was on the hydrogen-charging line, and point A was away from the line. Both local impedance plots were featured with two semicircles over the whole frequency range. In particular, there was a slightly bigger high-frequency semicircle at point B than that at point A, while the sizes of the low-frequency semicircles were similar. For the impedance plots containing two semicircles, it is generally accepted that the high-frequency semicircle is associated with the corrosion product layer or oxide film and the low-frequency one is related directly to the interfacial charge-transfer reaction. A big size of the semicircle indicates a high film resistance or charge-transfer resistance. Therefore, with the increase of the semicircle size, the corrosion resistance is enhanced.

3.3 SVET Measurements

Figure 4(a), (b), and (c) shows the SVET current density maps measured on the X100 steel specimen without hydrogen-charging and stressing, with hydrogen-charging only, and with stressing only in NS4 solution, respectively. Each SVET scan took about 20 min to complete. It is seen that there was a uniform current distribution when the electrode was not charged and stressed, with an average dissolution current density of 40 μA/cm^2 (Fig. 4a). When the specimen was charged at −1.2 V (SCE) for 1 h, with the charging line as indicated as the dotted line in Fig. 4(b), the current density ranged from the initial 80 to 65 μA/cm^2 by the end of the SVET scanning. However, there was no apparent change of current density around the hydrogen-charging line. When the specimen was loaded at 1000 N, the current density was uniformly distributed over the specimen, with an average of about 55 μA/cm^2. Moreover, no apparent change of current density was observed around the notch line, as marked by a dotted line in Fig. 4(c).

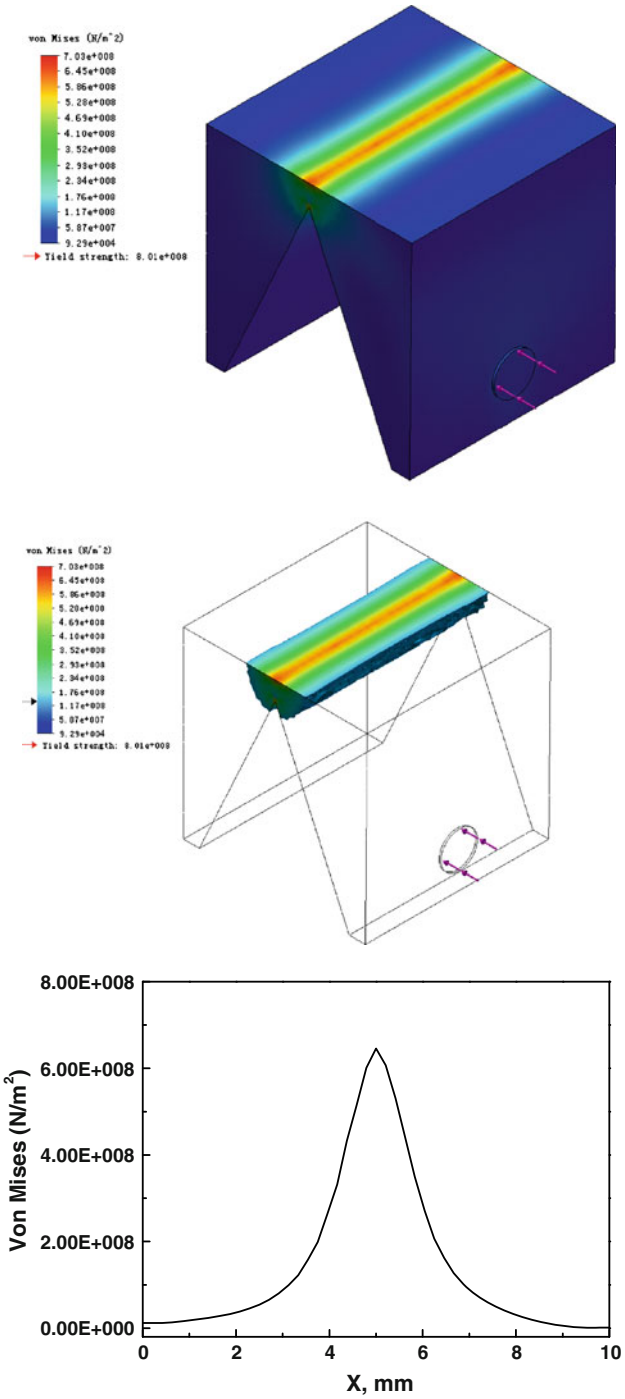

Fig. 2 Simulation and determination of stress distribution of the test specimen under a 1000 N of load

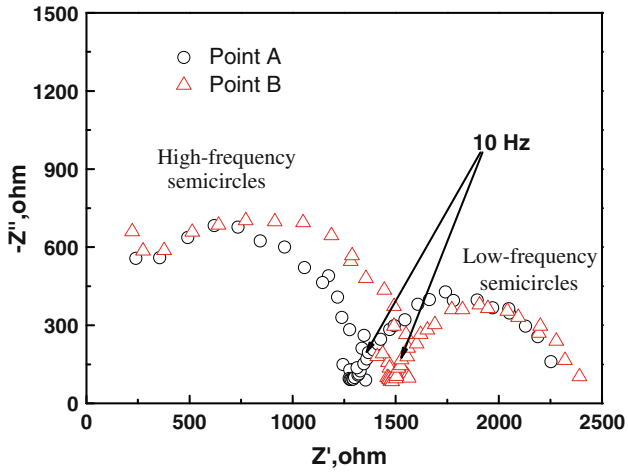

Fig. 3 LEIS plots measured at points A and B in Fig. 1

Figure 5 shows the SVET current density map measured on the X100 steel specimen with simultaneous loading at 1000 N and hydrogen-charging at −1.2 V (SCE) for 1 h in NS4 solution, where 3D and projected diagrams were given. The hydrogen-charging line was at $x = 1500$ μm, which was perpendicular to the notch line of $y = 1500$ μm. It is seen that there was a maximum of current density of about 350 μA/cm^2 near the point A of $x = 1500$ μm and $y = 1500$ μm.

4. Discussion

4.1 Effect of Hydrogen-charging on Anodic Dissolution of X100 Steel

Previous work (Ref 31, 32) has demonstrated that hydrogen-charging is capable of enhancing anodic dissolution of the steel, and the hydrogen effect is attributed to the alterations of chemical potential and exchange current density of the steel. Moreover, a layer of corrosion product, such as carbonate (Ref 31, 33), generated due to hydrogen accelerated corrosion reaction may form on the electrode surface to increase the measured impedance. The present work (Fig. 3) shows that two semicircles exist in the measured Nyquist diagram, with the high-frequency semicircle associated with the corrosion product layer and the low-frequency one with the interfacial charge-transfer reaction. Since the corrosion product layer is usually loose and porous (Ref 28), there is no much protection provided for the underlying steel. In Fig. 3, the slightly bigger size of the high-frequency semicircle measured at point B, which is on the hydrogen-charging line, than that at point A indicates that there is more or thicker corrosion product layer generated due to the hydrogen-enhanced corrosion. However, the approximately similar size of the low-frequency semicircles at points B and A shows that there is a similar charge-transfer resistance, and thus, the dissolution current density at the two points, which is caused by the rapid diffusion of the charged hydrogen atoms throughout the specimen.

Moreover, the hydrogen-enhancing dissolution rate of the specimen can also be demonstrated by the SVET measurements (Fig. 4a, b). Prior to hydrogen-charging, the average dissolution current density is about 40 μA/cm^2. Upon

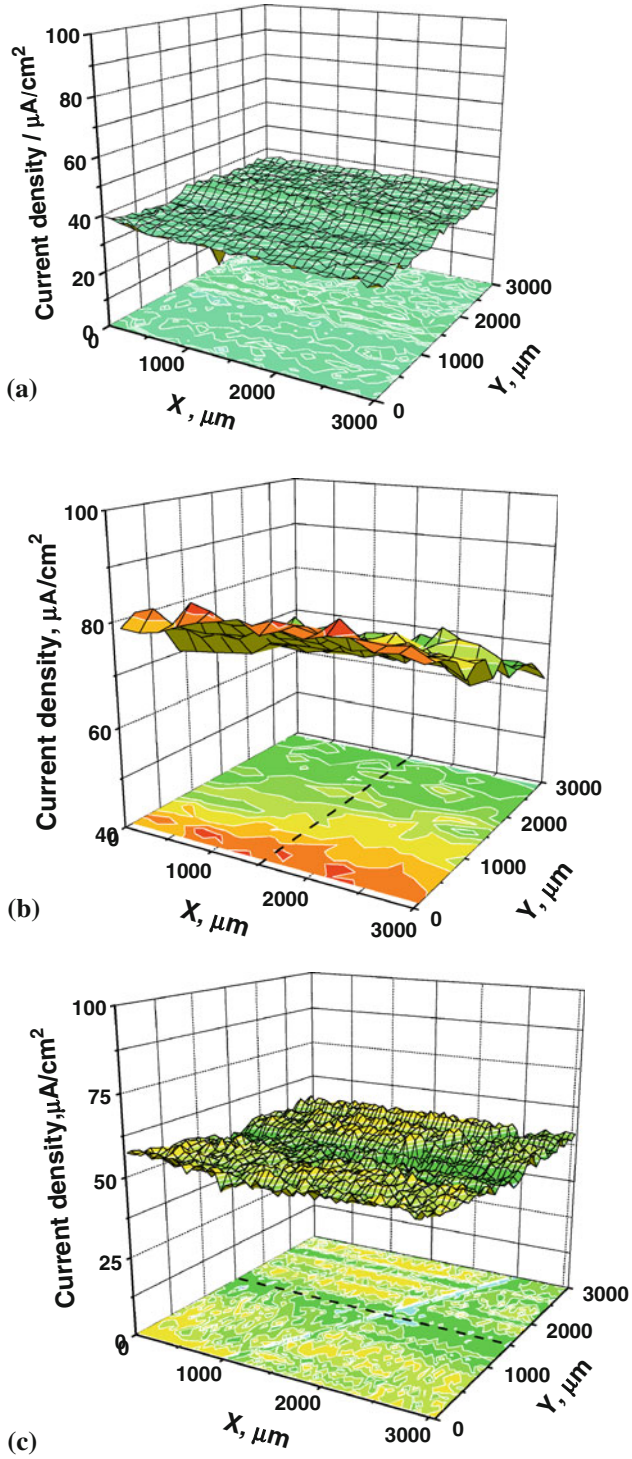

Fig. 4 SVET current density maps measured on specimen without hydrogen-charging and stressing (a), with hydrogen-charging (b), and with stressing (c) in NS4 solution

hydrogen-charging, the initial current density increases to 80 μA/cm^2, which is due to the hydrogen-enhanced corrosion reaction. With SVET measurement, the current density decreases to about 65 μA/cm^2, which is probably attributed to a gradual thickening of the corrosion product layer. However, the whole dissolution current density is much higher than that prior to hydrogen-charging.

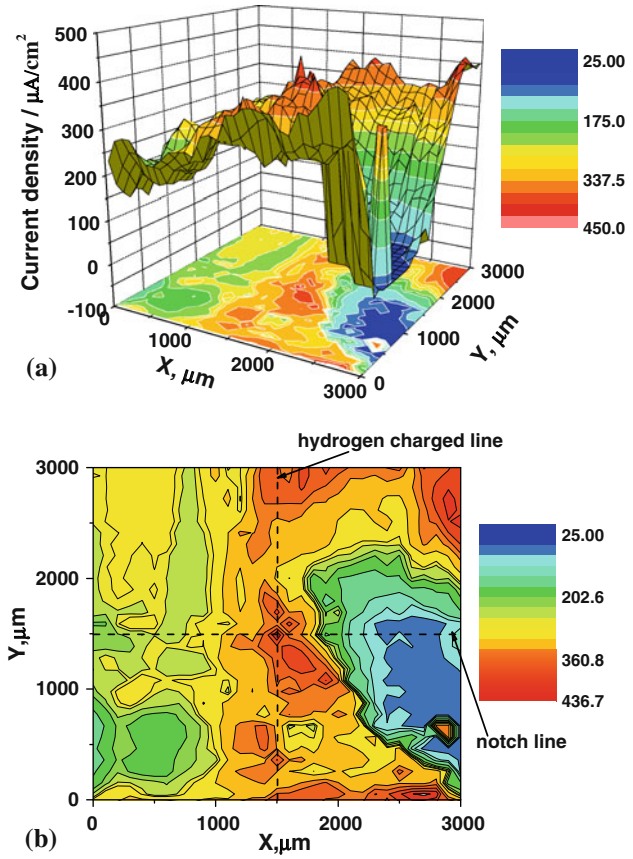

Fig. 5 SVME current density map measured in the presence of both stress and hydrogen-charging on the specimen in NS4 solution. (a) 3-dimensional plot; (b) equal-current density lines

4.2 Effect of Applied Stress on Anodic Dissolution of X100 Steel

The present work also shows that applied stress enhances anodic dissolution of the steel, as demonstrated in Fig. 4(a) and (c) by a comparison of the dissolution current densities measured before and after the applied loading of 1000 N. Since there is a stress concentration at the notch bottom, as seen in Fig. 2, it is expected that the local anodic dissolution at the notch is more significant than that at other region. However, the SVET current density scanning result in Fig. 4(c) shows that there is an approximately uniform distribution of current density over the whole scanning area, including both notched and other regions. The stress simulation in Fig. 2 shows that the maximum stress at the bottom of notch is about 640 MPa, which is much lower than the yielding strength of 820 MPa of the steel (Ref 34). It is generally believed (Ref 27) that, under a small tensile stress, the steel is in an elastic deformation status and the slip systems in the steel are not activated significantly. The steel is still in a relatively stable state. Therefore, the stress concentration alone in this work is not significant enough to result in an apparent increase of local dissolution rate of the steel.

4.3 Synergistic Effect of Hydrogen and Stress on Anodic Dissolution of X100 Steel

When the steel specimen is under simultaneous hydrogen-charging and applied loading, there is a significant increase of anodic current density, as seen in Fig. 4(c). Although the stress-enhanced activation is not sufficient to result in an apparent difference of current density at notch and at other area, the activation of the steel would activate dislocations, which serve as effective traps to the charged hydrogen atoms. With the increase of hydrogen concentration, the hydrogen-enhanced anodic dissolution becomes dominant. Therefore, even at a relatively small applied stress, the locally trapped hydrogen atoms are capable of enhancing remarkably the anodic dissolution of the steel.

5. Conclusions

The hydrogen-charging enhances the local anodic dissolution of the steel, contributing to the formation of a layer of corrosion product, which cannot provide effective protection over the underlying steel. There is little difference of the charge-transfer resistance between the regions with and without hydrogen-charging due to rapid diffusion of hydrogen atoms throughout the specimen with time.

Applied stress enhances anodic dissolution of the steel. When the local stress concentration is not significant enough to approach the yielding strength of the steel, the steel is still in a relatively stable state, and there is a uniform distribution of dissolution rate over the whole surface of the steel specimen.

Although the stress-enhanced activation is not sufficient to result in an apparent difference of current density of the steel, the activation of the steel would activate dislocations, which serve as effective traps to the charged hydrogen atoms. With the increase of hydrogen concentration, the hydrogen-enhanced anodic dissolution becomes dominant.

Acknowledgments

This work was supported by Canada Research Chairs Program, Natural Science Foundation of China (Project Nos. 50671007 and 50731003), and Chinese Scholarship Council.

References

1. K.T. Corbett, R.R. Bowen, and C.W. Petersen, High Strength Steel Pipeline Economics, *Int. J. Offshore Polar Eng.*, 2004, **14**, p 75–79
2. F.J. Sánchez, B. Mishra, and D.L. Olson, Magnetization Effect on Hydrogen Absorption in High-strength Steels and its Implications, *Scripta Mater.*, 2005, **53**, p 1443–1448
3. C. Kalwa, H.G. Hillenbrand, and M. Gräf, High-strength Steel Pipes: New Developments and Applications, *Onshore Pipeline Conference*, Houston, Texas, June 10-11, 2002
4. D. Porter, A. Laukkanen, P. Nevasmaa, K. Rahka, and K. Wallin, Performance of TMCP Steel with Respect to Mechanical Properties After Cold Forming and Post-forming Heat Treatment, *Int. J. Pressure Vessels Piping*, 2004, **81**, p 867–877
5. H.E. Minor, A. Kifani, M. Louah, Z. Azari, and G. Pluvinage, Fracture Toughness of High Strength Steel—Using the Notch Stress Intensity Factor and Volumetric Approach, *Struct. Saf.*, 2003, **25**, p 35–45
6. Y.Z. Wang, R.W. Revie, M.T. Shehata, R.N. Parkins, and K. Krist, Initiation of Environment Induced Cracking in Pipeline Steel: Microstructural Correlation, *International Pipeline Conference*, ASME, Calgary, 1998
7. W. Zheng, Stress Corrosion Cracking of High (or Low) Strength Steels: Preliminary Results and Relevance to New Pipeline Systems, *Presentations in the TransCanada Pipelines SCC Workshop*, Calgary, Sept 22, 2006

8. W. Zheng, D. Billy, J. Li, J.T. Bowker, J.A. Gianetto, R.W. Revie, and G. Williams, Studies of Stress Corrosion Cracking of X100 Steel by a Full Scale Test Apparatus, *Proceedings of the 2006 International Pipeline Conference*, IPC2006-10084, Calgary, Canada, Sept 25-29, 2006
9. M.A. Almonsour, "Sulfide Stress Corrosion Resistance of X100 Steel in H_2S Environments," MSc thesis, University of British Columbia, Vancouver, 2007
10. R.N. Parkins, A Review of Stress Corrosion Cracking of High Pressure Gas Pipelines, *Corrosion 2000*, NACE, Houston, 2000, Paper No. 363
11. B.Y. Fang, A. Atrens, J.Q. Wang, E.H. Han, Z.Y. Zhu, and W. Ke, Review of Stress Corrosion Cracking of Pipeline Steels in "Low" and "High" pH Solutions, *J. Mater. Sci.*, 2003, **38**, p 127–132
12. M. Baker Jr., Stress Corrosion Cracking Studies, *Integrity Management Program DTRS56-02-D-70036*, Department of Transportation, Office and Pipeline Safety, 2004
13. National Energy Board, Report of Public Inquiry Concerning Stress Corrosion Cracking on Canadian Oil and Gas Pipelines, MH-2-95, November 1996
14. Y.F. Cheng, Thermodynamically Modeling the Interactions of Hydrogen, Stress and Anodic Dissolution at Crack-tip During Near-neutral pH SCC in Pipelines, *J. Mater. Sci.*, 2007, **42**, p 2701–2705
15. C.W. Du, X.G. Li, P. Liang, Z.Y. Liu, G.F. Jia, and Y.F. Cheng, Effects of Microstructure on Corrosion of X70 Pipe Steel in an Alkaline Soil, *J. Mater. Eng. Perform.*, 2009, **18**, p 216–220
16. R.N. Parkins, W.K. Blanchards, Jr., and B.S. Delanty, Transgranular Stress Corrosion Cracking of High-pressure Pipelines in Contact with Solutions of Near Neutral pH, *Corrosion*, 1994, **50**, p 394–408
17. L. Niu and Y.F. Cheng, Corrosion Behaviour of X-70 Pipe Steel in Near-neutral pH Solution, *Appl. Surf. Sci.*, 2007, **253**, p 8626–8631
18. W. Bouaeshi, S. Ironside, and R. Eadie, Research and Cracking Implications from an Assessment of Two Variants of Near-neutral pH Crack Colonies in Liquid Pipelines, *Corrosion*, 2007, **63**, p 648–660
19. Y.F. Cheng and L. Niu, Mechanism for Hydrogen Evolution Reaction on Pipeline Steel in Near-neutral pH Solution, *Electrochem. Commun.*, 2007, **9**, p 558–562
20. B. Gu, J. Luo, and X. Mao, Hydrogen-facilitated Anodic Dissolution-type Stress Corrosion Cracking of Pipeline Steels in Near-neutral pH Solution, *Corrosion*, 1999, **55**, p 96–108
21. L.J. Qiao, J.L. Luo, and X. Mao, Hydrogen Evolution and Enrichment Around Stress Corrosion Crack Tips of Pipeline Steels in Dilute Bicarbonate Solution, *Corrosion*, 1998, **54**, p 115–120
22. L. Zhang, X.G. Li, C.W. Du, and Y.F. Cheng, Corrosion and Stress Corrosion Cracking Behavior of X70 Pipeline Steel in a CO_2-containing Solution, *J. Mater. Eng. Perform.*, 2009, **18**, p 319–323
23. T.M. Ahmed, S.B. Lambert, R. Sutherby, and A. Plumtrel, Cyclic Crack Growth of X-60 Pipeline Steel in a Neutral Dilute Solution, *Corrosion*, 1997, **53**, p 581–590
24. T.R. Jack, B. Erno, and K. Krist, Generation of Near-neutral pH and High pH SC Environments on Buried Pipelines, *Corrosion/2000*, NACE, Houston, TX, 2000, Paper No. 362
25. J.A. Beavers, C.L. Durr, B.S. Delanty, D.M. Owen, and R.L. Sutherby, Near-neutral pH SCC: Crack Propagation in Susceptible Soil Environments, *Corrosion/2001*, NACE, Houston, TX, 2001, Paper No. 217
26. R.R. Fessler and K. Krist, Research Challenges Regarding Stress Corrosion Cracking of Pipelines, *Corrosion/2000*, NACE, Houston, TX, 2000, Paper No. 370
27. X. Tang and Y.F. Cheng, Micro-electrochemical Characterization of the Effect of Applied Stress on Local Anodic Dissolution Behavior of Pipeline Steel Under Near-neutral pH Condition, *Electrochim. Acta*, 2009, **54**, p 1499–1505
28. G.Z. Meng, C. Zhang, and Y.F. Cheng, Effects of Corrosion Product Deposit on the Subsequent Cathodic and Anodic Reactions of X-70 Steel in Near-neutral pH Solution, *Corros. Sci.*, 2008, **50**, p 3116–3122
29. C.F. Dong, A.Q. Fu, X.G. Li, and Y.F. Cheng, Localized EIS Characterization of Corrosion of Steel at Coating Defect Under Cathodic Protection, *Electrochim. Acta*, 2008, **54**, p 628–633
30. X. Tang and Y.F. Cheng, Localized Dissolution Electrochemistry at Surface Irregularities of Pipeline Steel, *Appl. Surf. Sci.*, 2008, **254**, p 5199–5205
31. M.C. Li and Y.F. Cheng, Mechanistic Investigation of Hydrogen-enhanced Anodic Dissolution of X-70 Pipe Steel and its Implication on Near-neutral pH SCC of Pipelines, *Electrochim. Acta*, 2007, **52**, p 8111–8117
32. Y.F. Cheng and X. Tang, Micro-electrochemical Characterization of the Synergism of Hydrogen and Stress in Anodic Dissolution of Steel and its Implications on Pipeline Stress Corrosion Cracking, *Proceeding of the 6th International Pipeline Conference*, IPC2008-64142, Calgary, Canada, Sept 29 to Oct 3, 2008
33. M.Z. Yang, J.L. Luo, Q. Yang, L.J. Qiao, Z.Q. Qin, and P.R. Norton, Effects of Hydrogen on Semiconductivity of Passive Film and Corrosion Behavior of 310 Stainless Steel, *J. Electrochem. Soc.*, 1999, **146**, p 2107–2112
34. E. Sanjuan, "Studies of Corrosion and Stress Corrosion Cracking Behavior of High-strength Pipeline Steels in Carbonate/Bicarbonate Solutions," MSc thesis, University of Calgary, Canada, March 2008